Proceedings of ASME Turbo Expo 2011
GT2011
June 6-10, 2011, Vancouver, British Columbia, Canada

GT2011-45462

WAVELET ANALYSIS OF VORTICAL STRUCTURES IN TURBOMACHINERY APPLIED TO PIV DATA

Philipp Schaefer
Institute of Propulsion Technology
Turbine Department
German Aerospace Center (DLR)
Göttingen, 37073, Germany
Email: philipp.schaefer@dlr.de

Christian Cierpka
Institute of Fluid Mechanics and Aerodynamics
University of the German Armed Forces Munich
Neubiberg, 85577, Germany
christian.cierpka@unibw.de

Hans-Jürgen Rehder
Institute of Propulsion Technology
Turbine Department
German Aerospace Center (DLR)
Göttingen, 37073, Germany
Email: hans-juergen.rehder@dlr.de

Ingo Roehle
Institute of Propulsion Technology
Turbine Department
German Aerospace Center (DLR)
Göttingen, 37073, Germany
Email: ingo.roehle@dlr.de

ABSTRACT

In this paper the unsteady flow field of a highly loaded turbine rotor blade at different transonic Mach numbers by means of Particle Image Velocimetry (PIV) is investigated. The experiments are performed using the linear cascade wind tunnel at DLR Göttingen at isentropic exit Mach numbers 0.7, 0.9, and 1.1. The process of vortex shedding at the trailing edge of the blade and its proceeding downstream in the wake area is analyzed using a wavelet based vortex identification algorithm. The wavelet algorithm automatically detects vortices and extracts e.g. their position, their vorticity, and their convection velocity. This procedure enables a statistical analysis on the basis of numerous PIV recordings. The vortex production, the downstream transport and the vortex decay are observed successfully. The Strouhal number and the shedding frequency are directly derived from the vortex position and confirm previous investigations. The PIV combined with a wavelet based analysis constitutes a remarkable insight to time dependent flow structures.

NOMENCLATURE

c	chord lenght of the cascade [mm]
d_{TE}	diameter of trailing edge [mm]
D	spatial distance between two vortices [mm]
f	shedding frequency [kHz]
p	pressure [N/m^2]
u	downstream velocity [m/s]
κ	heat capacity ratio
Ma	Mach number
$Ma_{2,is}$	isentropic exit Mach number
RMS	root mean square
St	Strouhal number

INTRODUCTION

Unsteady flows in turbomachinery are evoked by the interplay of rotors and stators and their wakes. The downstream transport of turbulent wake structures and the influence on boundary layer transitions, on heat transfer, and on shocks was the focus of many studies [1–3]. However, experimental investigations on unsteady flows in turbomachinery remain a difficult task: a review by Cicatelli and Sieverding [4] reveals that often the spatial resolution of blades is limited due to small trailing edges. Furthermore, time-dependent wake turbulences along with local pressure and temperature variations result in a complex flow. While the limitation in resolution can be overcome by choosing large scaled blades, the latter needs to be carefully analyzed in the frequency domain to detect the different time scales. Modern measurement techniques, such as the Particle Image Velocimetry (PIV), offer the possibility to resolve the frequency spectrum of these turbulent, time-dependent structures [5, 6].

Using these methods, scientists often face a huge amount of data, which implies difficulties in handling or even a manual evaluation of the flow field. Effective ways of analyzing these flow fields are the use of transformation and decomposition methods, which filter the desired quantities. For instance, temporal Fourier Analysis can provide information about dominant frequencies, but gives no information about spatial occurrence of the extracted features. To overcome this limitation, the wavelet analysis automatically extracts the properties of vortices, such as size, vorticity and convection velocity. This method was already applied to several vortex dominated flows: in the case of flow control on a NACA0015 hydrofoil, the wavelet analysis helped to understand the individual vortex interaction above the suction side. By this, it enabled the optimization of the flow control parameter [7]. Furthermore, the algorithm was successfully used to investigate the flow generation process on a vibrating cantilever [8].

The present paper demonstrates the feasibility of the wavelet analysis to study typical turbomachinery flows and in particular to characterize the vortex structures. PIV frames are recorded at the trailing edge of a highly loaded turbine blade at sub-, trans-, and supersonic flow domains. The largest, visible turbulent structures appear in the von Karman vortex street, carrying most of the turbulent kinetic energy in the wake. The vortex position will be used for the analysis of the shedding frequency and the Strouhal number. For both values it will be shown that the wavelet analysis is an extremely efficient and precise tool. Furthermore, the vortex lifecycle, starting from the vortex production to dissipation, is recorded and investigated. The results contribute to a better determination of unsteady wake characteristics.

EXPERIMENTAL SETUP

Test Facility and Cascade Geometry

A schematic view of the wind tunnel for linear cascades (EGG) at DLR in Göttingen is given in Figure 1. The EGG is a blow-down facility with atmospheric inlet. The ambient air first enters a silica-gel dryer, subsequently passes two screens and a honeycomb flow straightener. After a contraction the flow enters

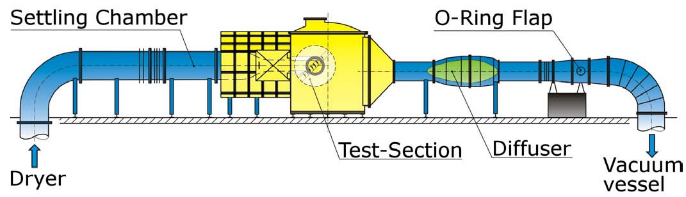

FIGURE 1. THE LINEAR CASCADE WINDTUNNEL (EGG)

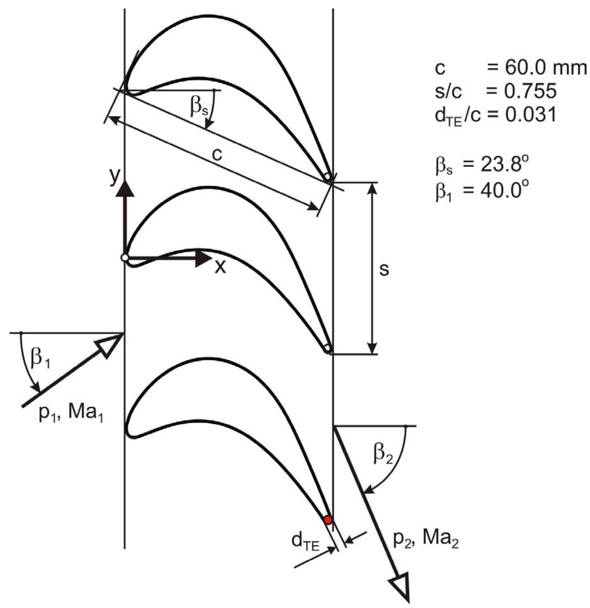

FIGURE 2. CASCADE GEOMETRY AND NOTATIONS

the cascade. Downstream of the test section the flow passes an adjustable diffuser and a fast opening valve. Finally, it enters a large vacuum vessel (10,000 m^3 capacity), which is evacuated by a set of pumps. The mass flow through the wind tunnel and hence the back pressure of the cascade is controlled by an appropriate setting of a choking diffuser. The pressure ratio of the static back pressure p_2 and the total pressure of the ambient air p_0 is used to calculate an isentropic exit Mach number $Ma_{2,is}$, which is the rig parameter to set the flow conditions in the test section.

$$Ma_{2,is} = \sqrt{\frac{2}{\kappa - 1}\left[\left(\frac{p_2}{p_0}\right)^{\frac{1-\kappa}{\kappa}} - 1\right]}, \tag{1}$$

with the heat capacity ratio κ. Due to constant (atmospheric) inlet conditions the Reynolds number cannot be varied independently, but is a function of the isentropic exit Mach number.

In the test section the cascade is mounted between two circular disks establishing the side walls of the flow channel. In order

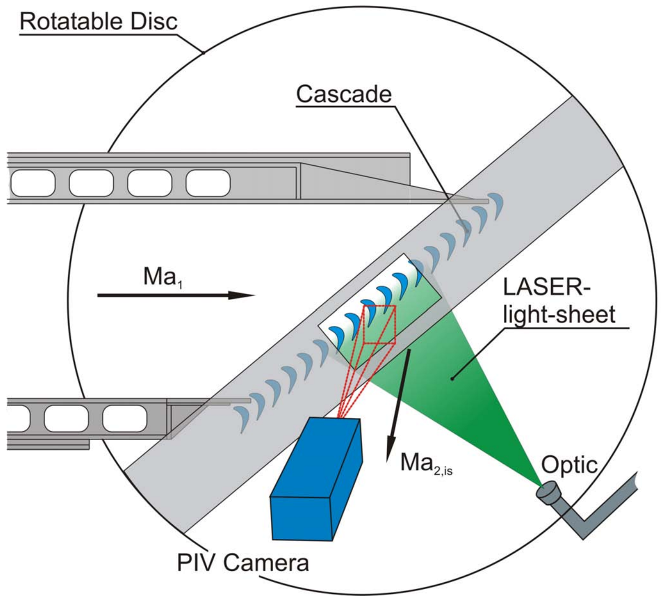

FIGURE 3. TEST SECTION WITH INTEGRATED PIV SETUP

to set a defined inlet angle the disks are rotatable. More details on this cascade wind tunnel can be found on the DLR webpage [9].

The cascade geometry is shown in Figure 2. This high pressure turbine airfoil with a relatively thick trailing edge denoted by d_{TE} is in particular designed for supersonic exit flow conditions and was extensively investigated at DLR [10, 11].

Particle Image Velocimetry (PIV)

Particle Image Velocimetry is applied following the rules given by Raffel et al. [12] to provide high quality data. The test section and the PIV setup is sketched in Figure 3. A planar PIV system manufactured by Lavision GmbH is used. It consists of a CCD camera, two seeding generators, a laser and light-sheed optics. A two-cavity Nd:YAG laser by New Wave generates two pulses with a diameter of $1\,mm$ and a power of $120\,mJ$ at a wavelength of $532\,nm$. The laser beams are guided by an optical arm and shaped into a light sheet of about $1\,mm$ thickness. The light sheet is then directed to the trailing edge of the turbine blade at midspan position. The axis of the camera (Flowmaster, PCO) is arranged perpendicular to the illuminated plane at a distance of about one meter. The camera is equipped with a NIKKOR 180/2.8 objective, the aperture 5.6 opened. The image sensor of the camera consists of a $1,280 \times 1,024\,px^2$ CCD-chip. This results in a spatial resolution of $0.045\,mm/px$ while the particle size is of about $2\,px$. Camera calibration is done with a target consisting of a known pattern.

The flow is seeded with tracer particles illuminated through the light-sheet. The particles (DEHS) are generated by two seeding ports with a total number of 90 Laskin nozzles operated at $0.5\,bar$ over-pressure. The seeding material of about $1\,\mu m$ is distributed homogeneously with a turbulence grid in the settling chamber, approximately four meters upstream of the test section. It is assumed that the injected massflow and the occurring turbulence from the grid has no influence on the test section.

The two succeeding laser pulses illuminate the seeded flow. Due to an appropriately chosen interval time for each exit velocity the mean displacement results in about $12\,px$. In this manner, 200 PIV frames are recorded for each $Ma_{2,is}$.

Evaluation of PIV

In order to enhance the quality of the raw pictures a sliding average of the background is subtracted. PIVview 3.0 from PivTec GmbH [13] is used to calculate the vector maps with a $24 \times 24\,px^2$ interrogation window size and 50% overlap. A multiple pass, multi-grid interrogation process with a window deformation algorithm is used for the calculation of the correlation [14, 15]. In addition, a three-point Gaussian peak fit is applied for sub-pixel resolution.

Each individual vector is validated by neglecting vectors with a predicted displacement higher than a given upper bound of $18\,px$, and by a minimum correlation of 20%. Furthermore, the vector is compared to its eight surrounding neighbors by first a normalized median test [16] and second by a vector difference test. Suspicious vectors are replaced by re-evaluating with a larger sample size from the previous multigrid iteration, by trying lower order peaks and at last by interpolation. Using this protocol, an average of about 97% of all calculated vectors are classified to be valid, which finally yields 79×63 sized vector maps.

A central difference scheme is applied to calculate the velocity derivatives. The central difference method is known to reduce the effect of random errors due to slightly smoothing the vorticity distributions [12].

Error Analysis of PIV

The assessment of the uncertainty in PIV data is a difficult task when dealing with unsteady flows. Fluctuations in the calculated velocity components are composed of the unsteady flow behavior and the error of the velocity estimation. The latter is due to the evaluation algorithm and the particle's inertia. Both errors are assumed to reach a maximum at $Ma_{2,is} = 1.1$ and are discussed in the following.

In the current study, a multi-pass multi grid window shifting method is applied to evaluate the experimental images. The peak in the correlation plane is determined with sub-pixel accuracy by a three-point Gaussian peak fit. Typically, more than 10 particles with a mean diameter of $2\,px$ are found in each interrogation window. The uncertainty of the applied methods under these conditions is below $0.06\,px$ [12]. Considering the maximum time delay of $\Delta t = 1\,\mu s$, this results in an uncertainty of the

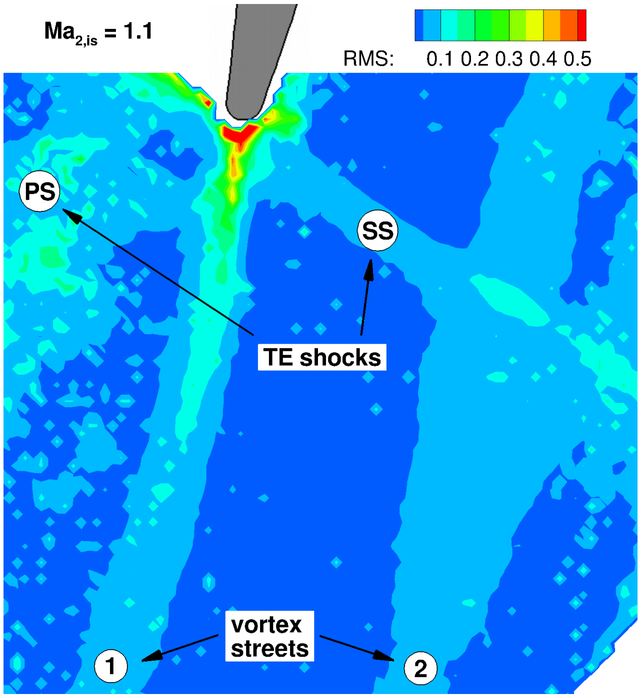

FIGURE 4. RMS VALUE OF THE VELOCITY MAGNITUDE CALCULATED FROM 200 PIV MAPS. THE VORTEX STREETS AND THE TRAILING EDGE SHOCKS CONTRIBUTE TO HIGH FLUCATIONS DUE TO THEIR UNSTEADY FLOW BEHAVIOR

velocity of $2.7\,m/s$ or about 0.7% of the velocity at $Ma_{2,is} = 1.1$.

In Figure 4 the RMS value of the velocity magnitude from 200 PIV recordings is illustrated. In the area between the two vortex streets the flow is nearly steady. The RMS value remains at a low level ($RMS < 0.03$). It is assumed that only the error of the velocity estimation contributes to the fluctuations. Thus, the overall uncertainty of the velocity magnitude amounts about $6\,m/s$, which is in good agreement with the estimation given in [12]. Higher RMS values at the trailing edge, the vortex streets and the shocks imply the unsteadiness of the flow and are not a measurement error.

The uncertainty of the velocity contributes to the uncertainty of the vorticity magnitude since the vorticity field is calculated from the velocity vector field. A central difference scheme is employed in order to approximate the first order differentials. The uncertainty of this method is 0.7 times the error of the velocity estimation divided by the grid size [12]. Furthermore, the uncertainty of the vorticity doubles since two derivatives are used. Using the above error estimation of the velocity, the uncertainty of the vorticity is of the order $13,000\,s^{-1}$.

In addition, the spatial resolution of the vortices is prescribed by the given grid size. The observed vortices vary between 3×3 and 7×7 of the grid size. The true vorticity magnitude is not recovered by this insufficient spatial resolution. Therefore, the vorticity magnitude has to be interpreted qualitatively. Nevertheless, the vortex position is estimated at a maximum error of the grid size and thus the error is lower than $0.54\,mm$. The vortex convection velocity is consequently calculated from the velocity vector map and is therefore independent of any vorticity error.

The particles inertia is the main source of uncertainty in the vicinity of the shock since the particles are not able to follow the flow instantaneously. Following [12], the time necessary to decelerate a $1\,\mu m$ particle over a shock is calculated to be in the order of $6\,\mu s$. The influence on the vorticity magnitude is negligible since the time difference between two PIV frames is six times lower. Furthermore, it is recognized that suction side shock occurs perpendicular to the vortex street 2 (see Figure 4), which means that all vortices passing through the shock are uniformly decelerated over the shock.

This error analysis reveals that the velocity estimation and the determination of the vortex position are of high accuracy. A precise value of the latter is needed in order to calculate the Strouhal number accurately. Due to the lack of spatial resolution, the recovered vorticity magnitude has to be interpreted qualitatively.

Wavelet Analysis

The applied wavelet algorithm was originally proposed by Schram [17], which is based on the enstrophy distribution. In contrast to this, the present algorithm uses the vorticity of the flow field. It has been successfully applied to problems in hydrodynamic research [7, 8]. The wavelet algorithm uses a two-dimensional Marr wavelet, also known as Mexican hat, to analyze the vorticity fields determined from the velocity fields. A spatial Gaussian distribution of the vorticity is often found for the shed vortices and holds as long as the deformation due to shear or wall influences is low. This assumption allows the calibration of the algorithm with the theoretical model of the Lamb-Oseen vortex [18]. The different vortex characteristics such as spatial position, vortex size, circulation, trajectories, and averaged convection velocities are extracted.

In order to ensure the reliability of the detected structure to be a vortex, the absolute value of the wavelet coefficient is calculated from the experimental data. It depends on the size of the vortex and its vorticity. The ratio between the detected wavelet coefficient and the theoretical one is calculated with the maximum vorticity at the center of the structure. In the following, this criterion was set to have an agreement of at least 85% between the Lamb-Oseen vortex model and the detected structure.

In order to distinguish between the coherent structures and the shear layer, the λ_2-criterion, as proposed by Jeon and Hussain [19] was used. This criterion is based on the second highest eigenvalue of the velocity gradient tensor and is widely ac-

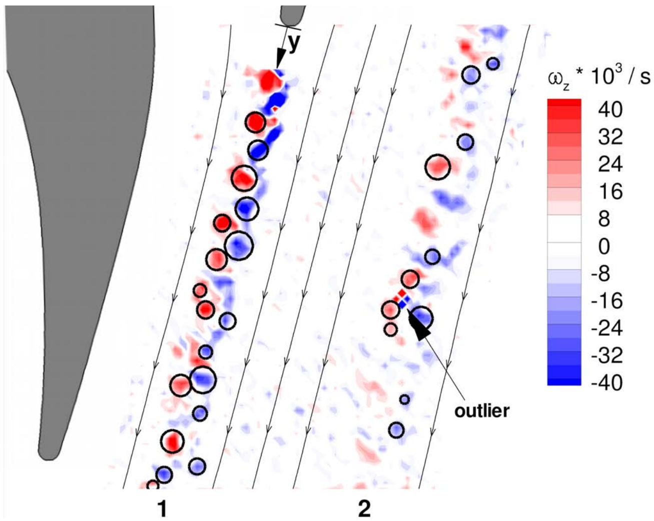

FIGURE 5. SINGLE VORTICITY FIELD WITH STREAMLINES INDICATING THE MAIN FLOW DIRECTION. BY THE WAVELET ALGORITHM DECTECTED VORTICES ARE MARKED BY A CIRCLE. THE ORIGIN IS LOCATED AT THE TRAILING EDGE OF BLADE 1 WITH Y DENOTING THE MAIN FLOW DIRECTION.

cepted in fluid dynamic research. If the λ_2-criterion is met, i.e., for $\lambda_2 < 0$, a vortex is expected since the rotational part of the velocity gradient tensor is bigger than the one due to deformation. To determine the best possible choice for the wavelet scales, the wavelet algorithm computes the size of potential structures in advance by summing up connected regions of negative λ_2. It adjusts the range of scales which are used in the transformation. By applying this procedure a more precise scale detection is achieved, which increases the resolution and saves computational time. For more details on the implementation the interested reader is referred to [20].

RESULTS AND DISCUSSION

Wavelet Analysis Applied to a Single Vorticity Field

In Figure 5 an instantaneous vorticity field recorded by PIV is illustrated. The direction of the main flow is indicated by the drawn streamlines. The two visible vortex streets are denoted by 1 and 2. In the main flow direction alternating vortices shed from the pressure and suction side at 180° out of phase. This flow behavior is confirmed by the Schlieren visualization in Figure 6.

As expected, the vortex intensity declines with increasing distance to the trailing edge. Nearby the trailing edge of the blade, suction side vortices appear to be kidney-shaped and differ significantly from the Lamb-Oseen vortex. A similar behavior is observed by Woisetschläger [22] and Carscallen [23]. Since only a few outliers are visible, it can be assumed that the filter parameters of the outlier detection are properly set.

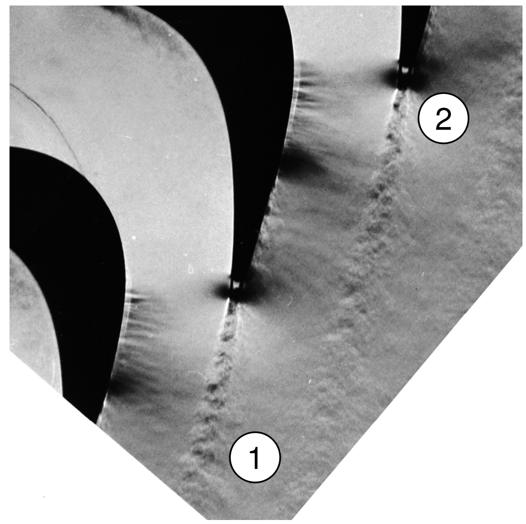

FIGURE 6. SCHLIEREN PICTURE OF SUBSONIC FLOW DOMAIN AND THE VISIBLE VON KARMAN VORTEX STREET [21]

As discussed in the previous section, the wavelet analysis stores for each vortex core the position, the size of the vortex core, the vorticity and the convection velocity. By applying this wavelet algorithm to the flow fields shown in Figure 5, vortex structures are now detected automatically. The found vortices are marked by circles: the center of the latter indicates the position of the vortex and its diameter corresponds to the vortex core. It is found that the alternating structure of the vortices is perfectly detected in the first vortex street. Due to the appropriately chosen wavelet scale, this is valid not only for the symmetric, but also for the asymmetric vortices, which do not coincide to the Mexican hat wavelet. On the second vortex street a lot of the vortical structures are detected. With increasing distance to the trailing edge, however, the vortex detection rate declines. The reason is found from two aspects: First, the rotational energy is transferred to widely spread smaller substructures and the overall vorticity decreases. Second, the calibration of the wavelet scale is not suitable to detect vorticity scales lower than roughly $10,000\,s^{-1}$, which is the intensity of the substructures in the vortex street 2. As additionally to be seen in Figure 5, the extant outliers are significantly smaller in size than a common vortex and this is why the outliers are correctly neglected by the wavelet algorithm.

The discussion on the single PIV frame already demonstrates the usefulness of the wavelet analysis to filter vortices from instantaneous vector fields. A *comprehensive* description of the vortex shedding process requires numerous recordings at different flow phases and a subsequent ensemble evaluation.

Figure 7 shows the complete ensemble at $Ma_{2,is} = 0.7$ of the 200 PIV recordings. The flow field is divided into three main areas: these are the two vortex streets corresponding to the num-

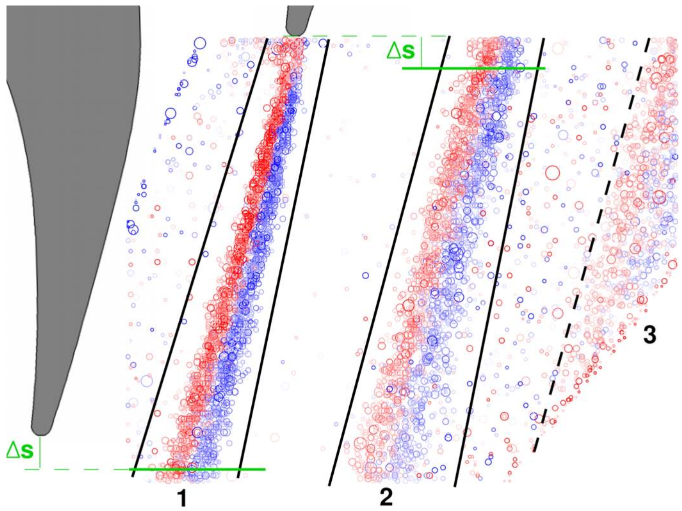

FIGURE 7. DETECTED VORTICES FROM 200 PIV VECTOR FIELDS AT $Ma_{2,is} = 0.7$. THE CIRCLE SIZE CORRESPONDS TO THE CORE VORTEX DIAMETER AND THE COLORS TO THE VORTICITY

bers in Figure 5 and 6. The dashed line separates the wake flow of the neighboring third blade, which is not taken into account furthermore. A spatial filter is applied as indicated by black lines enframing the first two wake flows. In this way, all vortices that do not belong to the wakes 1 and 2 are excluded from the analysis.

Nearby the trailing edge a contraction of the flow can be seen where the suction and pressure side flow merge. Further downstream, the wake expands to a point where the suction and pressure side vortices can be clearly distinguished.

A suitable distance Δs between two neighboring trailing edges is chosen and marked by green lines in Figure 7. This enables the continuation of the Karman vortex street from the first blade to the second assuming periodic flow conditions within the straight cascade. On the second vortex street the detection density drops in flow direction due to dissipation. It is recognized that the pressure side vortices seem to survive longer than vortices from the suction side. A physical reason might be the fact that boundary layer is usually smaller on the pressure side: this leads to a thinner shear layer and thus to a higher velocity gradient between the pressure side boundary layer and the dead water. Since the shear layer is the driver of the vorticity, the vorticity magnitude is higher, which leads to a longer lasting vortex street on the pressure side.

In the following sections the vortex distance derived from the vortex position, the convection velocity, and the vorticity are statistically investigated at $Ma_{2,is} = \{0.7, 0.9, 1.1\}$.

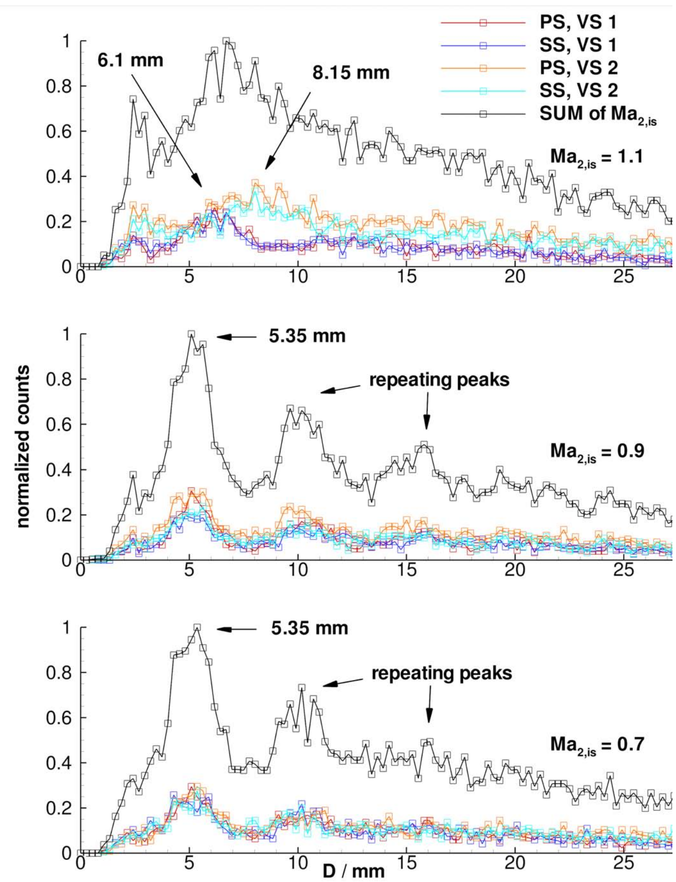

FIGURE 8. NORMALIZED HISTOGRAM OF THE VORTEX DISTANCE DISTRIBUTION. THE COLORED CURVES REPRESENT THE SUCTION AND PRESSURE SIDE PART OF VORTEX STREETS 1 AND 2, THE BLACK LINE GIVES THE SUM

Vortex Shedding Frequency and Strouhal Number derived from the Vortex Distances

Since two neighboring vortices of the same rotational sense have the same phasing, the vortex shedding frequency f can be estimated from $f = u/D$, with u denoting the downstream velocity derived from $Ma_{2,is}$ while D represents the distance of two vortices. The vortex distance is calculated between two vortices of the same rotational sense and originating from the same vortex street. Afterwards, the distance is rounded to integer pixel values leading to a maximum spatial error of about $0.0223\,mm$. This yields four histograms (colored) for each Mach number and their sum (black). All curves are drawn with an average over $8\,px$ in Figure 8.

At $Ma_{2,is} = \{0.7, 0.9\}$ the shape of D from suction and pressure side as well as for each vortex street have their peaks at about the same position. Therefore, the global peak of the sum is accentuated. The prevalent displacement of both Mach num-

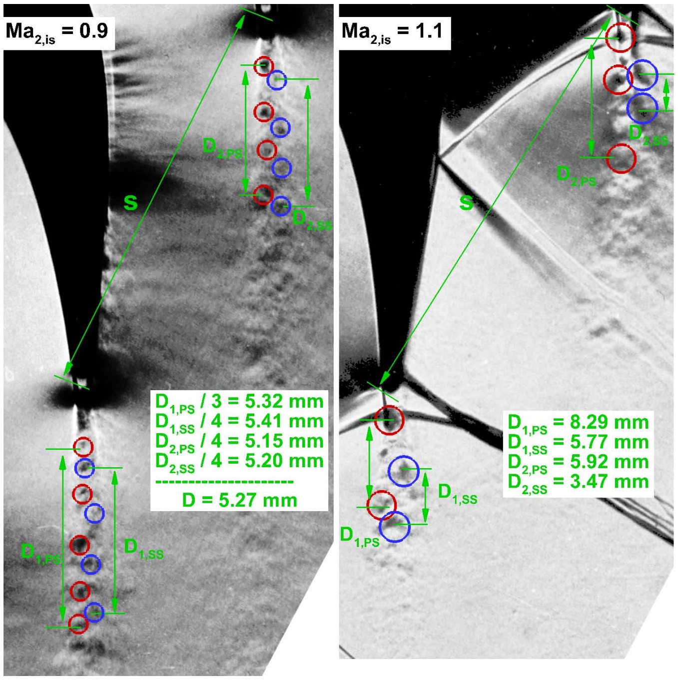

FIGURE 9. VORTEX DISTANCES MEASURED BY MANUAL INSPECTION AND AVERAGED OVER THE DETECTED VORTICIES, WHICH ARE MARKED BY CIRCLES [21]

bers is located at about $5.35\,mm$. This is further supported by the appearing peaks at multiples of this distance.

At supersonic flow conditions, the peak is not as clear as in the subsonic domain. While the dominant distance from vortex street 1 is at about $6.1\,mm$, the second vortex street has a widely spread maximum at about $8.15\,mm$. Vortex street 2 has already passed through the trailing edge shock seen in the Schlieren picture in Figure 11. The broad peak of the second vortex street is a result of a higher fluctuation in the counted distances due to the discussed limitation of PIV: tracer particles cannot instantaneously follow the deceleration over a shock due to their inertia. Furthermore, the oscillating shock leads to a further noise in the vortex distance. To the author's knowledge, this effect has not been recorded before, as in previous studies the prevalent distance was measured only close to the trailing edge [4]. Thus, to allow for comparison, the peak of vortex street 1 is assumed to be the prevalent distance at $Ma_{2,is} = 1.1$.

In order to confirm the prevalent distances found by the wavelet algorithm, two Schlieren pictures are manually inspected. The measured distances are presented in Figure 9 and averaged over the counted vortices, where the spacing s is used to calculate the true length. At $Ma_{2,is} = 0.9$ the average distance amounts $5.27\,mm$, which is nearly the prevalent vortex distances found by the wavelet algorithm. At supersonic flow only a few vortices can be recognized as it is difficult to distinguish between vortex cores and turbulences. Nevertheless, the measured distances $D = \{3.47\,mm, 5.92\,mm, 8.29\,mm\}$ are the main peaks, which are found by the wavelet analysis (see Figure 8). This comparison demonstrates that the wavelet analysis accurately resolves the dominant vortex distances.

TABLE 1. RESULTING STROUHAL NUMBERS AND SHEDDING FREQUENCIES FROM VORTEX DISTANCES ANALYSIS

$Ma_{2,is}$	vortices	$u\ [m/s]$	$D\ [mm]$	$f\ [kHz]$	St
0.7	4,224	229.6	5.35	34.8	0.34
0.9	4,717	287.1	5.35	43.5	0.34
1.1	3,968	338.8	6.1	55.5	0.30

The Strouhal number St is calculated by

$$St = \frac{f \cdot d_{TE}}{u} = \frac{d_{TE}}{D}, \tag{2}$$

and can be computed directly from the prevalent vortex distance. The resulting shedding frequencies as well as the Strouhal numbers are listed for all $Ma_{2,is}$ in Table 1. In addition, the total number of detected vortices and the downstream velocity are included.

The results given by Cicatelli and Sieverding [4] are confirmed, because at $Ma_{2,is} = \{0.7, 0.9\}$ the Strouhal number remains constant while the shedding frequency increases. Similar airfoils are investigated in [24, 25] confirming the Strouhal number to be constant with a linear increase of the shedding frequency for the subsonic domain. Furthermore, the Strouhal number in [24] ranges between 0.31 and 0.35 for airfoils of the same chord length and similar trailing edges at $Ma_{2,is} = \{0.7, 0.9\}$. The tendency of an increasing St in [4] at supersonic flow conditions cannot be supported. Although it is difficult to determine the dominant distance at $Ma_{2,is} = 1.1$, a decrease of the Strouhal number is more likely. The same behavior was found in [25].

Strouhal numbers between 0.23 and 0.35 indicate a transitional boundary layer state on one or both sides of the blade [4]. In the supersonic domain transition is observed on the suction side: in the Schlieren picture (Figure 11) the trailing edge shock causes transition on the neighboring blade suction side. At $Ma_{2,is} \leq 0.9$ boundary layer as well as surface pressure measurements reported in [26] show a strong adverse pressure gradient near by the throat area. For this, transition occurs on the suction side confirming a transitional boundary layer state.

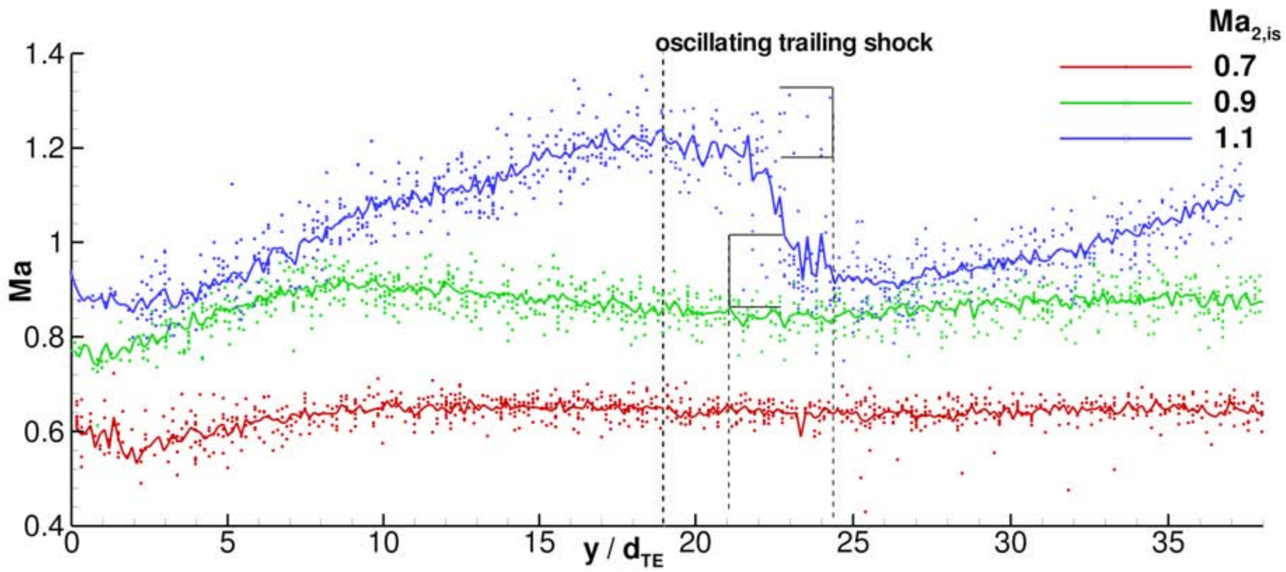

FIGURE 10. VORTEX MACH NUMBER OVER THE DISTANCE FROM THE TRAILING EDGE

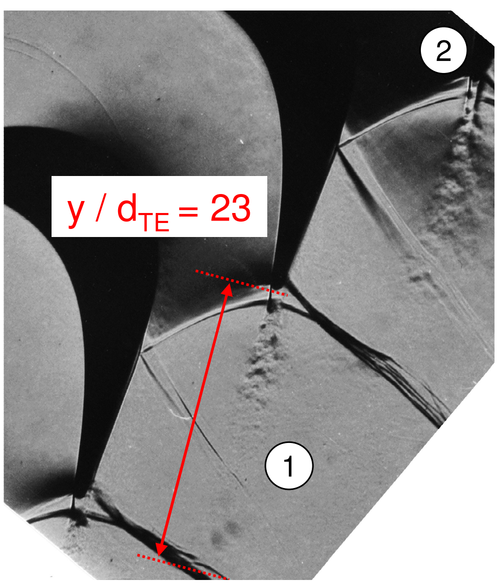

FIGURE 11. SCHLIEREN PICTURE AT $Ma_{2,is} = 1.1$ [21]

Convection Velocity

In the following two sections the evolution of the vortices will be investigated statistically. Figure 10 displays the convection velocity. The coordinate system is taken as sketched in Figure 5. The length is scaled by the trailing edge thickness d_{TE}. In order to guide the eye the arithmetic mean of the data in an interval $\Delta y/d_{TE} = 0.3$ is shown. In addition, only every fourth data point is drawn to keep a clear view.

Close to the trailing edge vortices separate from the boundary layer and are accelerated by the main flow, which is seen in the increase of the local Mach number. In the subsonic case the speed reaches a constant value of about $Ma = 0.65$, which is 0.03 less than the mixed out free stream velocity derived from wedge probe measurements [26]. For trans- and supersonic flow regimes the vortices pass through areas where expansion fans and shocks occur. Thus, the vortex's Mach number is increased or decreased, respectively.

At supersonic flow conditions it is clearly visible that the vortices are accelerated due to the expansion fan caused by the neighboring blade's suction side. At $y/d_{TE} = 23$, which is approximately the spacing s of the linear cascade, the trailing edge shock causes a decline from 1.2 to 0.85 of the vortex Mach number. After the shock the vortices are accelerated well above $Ma = 1.0$ by the next expansion fan.

At the trailing edge shock an overlap of data points located in front and behind the shock is observed. This overlap is explained by the oscillating movement of the shock at the trailing edge. The minimum and maximum shock position can be deduced using the information of vortex position. The trailing edge shock varies between $y/d_{TE} = [21; 24.5]$ as indicated by the brackets in Figure 10. At the same position in the Schlieren picture given in Figure 11 the trailing edge shock is observed.

Furthermore, at $Ma_{2,is} = 0.9$ a weak shock located on the suction side causes a decrease at $y/d_{TE} = 15$. As discussed in the previous section, the broaden of the shock is caused by the inertia of the tracer particles.

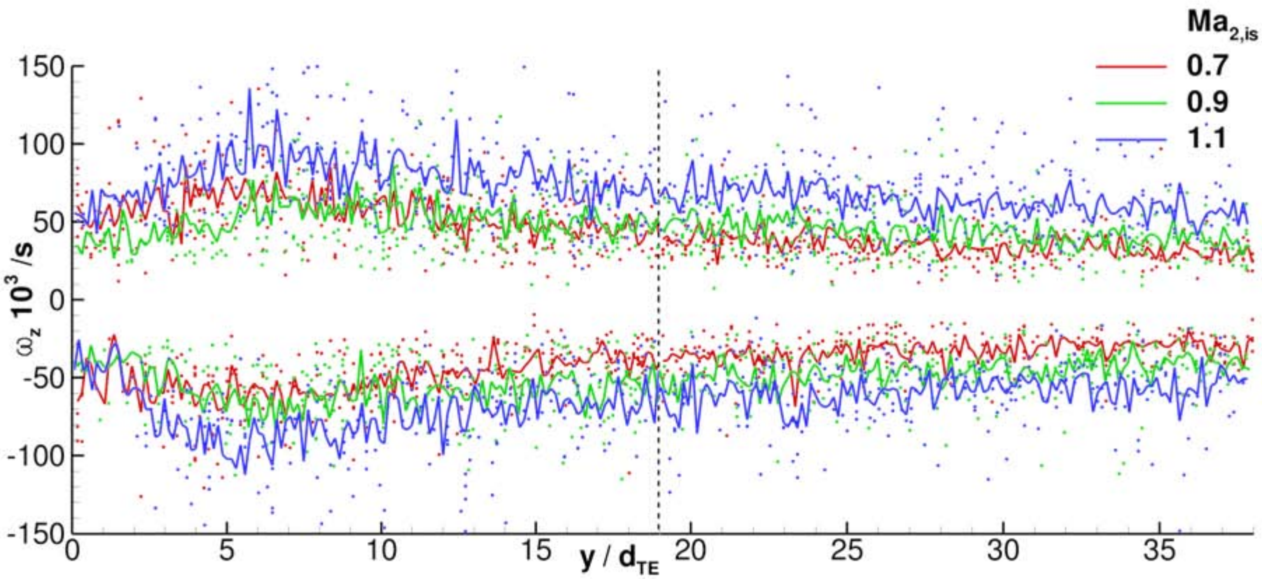

FIGURE 12. VORTICITY OVER THE DISTANCE FROM THE TRAILING EDGE

Vorticity

The data shown in Figure 12 is analogously organized as in Figure 10. Positive vorticity values belong to the pressure side and rotate in counterclockwise direction. Vortices shed from the suction side have a clockwise spin and therefore a negative vorticity.

At the wake position ($y/d_{TE} = 0$) the absolute value of vorticity amounts about $50,000s^{-1}$ and increases due to the strong gradient between the wake area and the main flow. Two shear layers are formed: one between the dead water and the suction side flow and the second between the dead water and the pressure side flow. The thickness of these shear layers depend on the boundary layer state and are the most important driver for the increase of vorticity. Furthermore, an increase of $Ma_{2,is}$, which also increases the overall Mach number distribution around the blade, leads to higher vorticity values. At the point, where the flow from suction side and pressure side merge, vorticity reaches its maximum at $y/d_{TE} \approx 6$. The union of the flow is the end of the dead water, which means that the shear layers perish. Beyond this point no shear layer exists anymore that transfers kinetic energy into the rotation of the vortices. Therefore, vorticity starts to decrease continuously in all flow regimes, which implies dissipation and entropy production.

At all $Ma_{2,is}$ high fluctuations are observed, which have been discussed in the section of the error analysis. Therefore, the presented vorticity values have to be interpreted qualitatively and cannot be directly compared to other data, e.g. unsteady numerical simulations. In order to overcome this deficiency measurements at higher resolution are a focus of future work.

CONCLUSION AND OUTLOOK

Particle Image Velocimetry was successfully applied to unsteady turbomachinery flow at realistic Mach numbers. In particular, the von Karman vortex street was recorded over a long range. The postprocessing of the data was performed by the wavelet analysis leading to a proper description of the vortex position and convection velocity. Thereby, the wavelet analysis was a very effective way to extract and analyze vortical structures. This enabled a statistical analysis of the flow fields. The spatial position deduced from numerous vortices enabled the calculation of the Strouhal number and the shedding frequency. These were in excellent agreement with previous measurements. Furthermore, the convection velocity confirmed a typical flow behavior at sub- and supersonic flow conditions. Due to a lack of spatial resolution the vorticity values are biased, which can be easily overcome by a higher spatial resolution. Nevertheless, the wavelet analysis gives a remarkable insight to turbomachinery flows.

In order to improve the detection rate of the wavelet analysis, an elliptic basis rather than the presently used basis of rotational symmetry should be developed, which is capable to detect kidney-shaped vortices. Besides the aim to improve the resolution of the PIV system, a second task is to reduce the particle lag, which can be resolved by choosing particles smaller in size. With these improvements the wavelet analysis together with the PIV system can be a promising tool to allow for direct comparison of experimental data to numerical simulations and pave the way for further model developments.

REFERENCES

[1] Schulte, V., and Hodson, H., 1998. "Unsteady wake-induced boundary layer transition in high lift LP turbines". *Journal of turbomachinery,* ***120***, p. 28.

[2] Du, H., Han, J. C., and Ekkad, S. V., 1998. "Effect of unsteady wake on detailed heat transfer coefficient and film effectiveness distributions for a gas turbine blade". *Journal of turbomachinery,* ***120***, p. 808.

[3] Hummel, F., 2002. "Wake–wake interaction and its potential for clocking in a transonic high-pressure turbine". *Journal of Turbomachinery,* ***124***, p. 69.

[4] Cicatelli, G., and Sieverding, C. H., 1996. "A review of the research on unsteady turbine blade wake characteristics". *Rhode-Saint-Genese, Belgium: von Karman Institute for Fluid Dynamics*.

[5] Göttlich, E., Woisetschläger, J., Pieringer, P., Hampel, B., and Heitmeir, F., 2006. "Investigation of vortex shedding and wake-wake interaction in a transonic turbine stage using laser-doppler-velocimetry and particle-image-velocimetry". *Journal of Turbomachinery,* ***128***, p. 178.

[6] Voges, M., Schnell, R., Willert, C., Mönig, R., Müller, M. W., and Zscherp, C., 2011. "Investigation of Blade Tip Interaction With Casing Treatment in a Transonic Compressor, Part I: Particle Image Velocimetry". *Journal of Turbomachinery,* ***133***, p. 011007.

[7] Cierpka, C., Weier, T., and Gerbeth, G., 2010. "Synchronized force and PIV measurements for active flow control on a NACA0015 in post stall by periodic electro-magnetic forcing". *Physics of Fluids,* ***22***.

[8] Kim, Y., Cierpka, C., and Wereley, S. T., 2011. "Flow field around a vibrating cantilever: Coherent structure eduction by continuous wavelet transform and proper orthogonal decomposition". *Journal of Fluid Mechanics*. accepted for publication.

[9] DLR, 2010. DLR website. On the WWW, Oct. see URL `http://www.dlr.de/at/en/`.

[10] Dietrichs, H. J., Hourmouziadis, J., Malzacher, F., and Braunling, W., 1987. "Flow phenomena in transonic turbine cascade detailed experimental and numerical investigation". In Air breathing engines: 8th International symposium: Papers, American Institute of Aeronautics and Astronautics, p. 425.

[11] Michelassi, V., Rodi, W., and Gieß, P.-A., 1999. "Experimental and numerical investigation of boundary layer and wake development in a transonic turbine cascade". *Aerospace Science and Technology,* ***2***, pp. 191–204.

[12] Raffel, M., Willert, C., Wereley, S. T., and Kompenhans, J., 2007. *Particle Image Velocimetry, A practical guide (2nd Edition)*. Springer Verlag, Berlin-Heidelberg.

[13] PivTec GmbH, 2010. PIVview 3.0. On the WWW, Oct. see URL `http://www.pivtec.de/`.

[14] Scarano, F., and Riethmuller, M. L., 1999. "Iterative multigrid approach in PIV image processing with discrete window offset". *Experiments in Fluids,* ***26***(6), pp. 513–523.

[15] Scarano, F., 2002. "Iterative image deformation methods in PIV". *Measurement Science and Technology,* ***13***, p. R1.

[16] Westerweel, J., and Scarano, F., 2005. "Universal outlier detection for PIV data". *Experiments in Fluids,* ***39***(6), pp. 1096–1100.

[17] Schram, C., Rambaud, P., and Riethmuller, M. L., 2004. "Wavelet based eddy structure eduction from a backward facing step flow investigated using particle image velocimetry". *Experiments in Fluids,* ***36***(2), pp. 233–245.

[18] Lamb, H., 1932. *Hydrodynamics*, 6 ed. Cambridge University Press. (first paparback edition 1993).

[19] Jeong, J., and Hussain, F., 1995. "On the identification of a vortex". *Journal of Fluid Mechanics,* ***285***, pp. 69–94.

[20] Cierpka, C., Weier, T., and Gerbeth, G., 2008. "Evolution of vortex structures in an electromagnetically excited separated flow". *Exp Fluids,* ***45***, pp. 943–953.

[21] Bräunling, W., 1987. IB 222 - 87 a 26. Internal Report.

[22] Woisetschläger, J., Mayrhofer, N., Hampel, B., Lang, H., and Sanz, W., 2003. "Laser-optical investigation of turbine wake flow". *Experiments in Fluids,* ***34***(3), pp. 371–378.

[23] Carscallen, W. E., Currie, T. C., Hogg, S. I., and Gostelow, J. P., 1999. "Measurement and computation of energy separation in the vortical wake flow of a turbine nozzle cascade". *Journal of Turbomachinery,* ***121***, p. 703.

[24] Heinemann, H.-J., and Bütefisch, K. A., 1978. "Determination of the vortex shedding frequency of cascade with different trailing edge thickness". *AGARD Unsteady Aerodyn. 11 p(SEE N 78-22033 13-02)*.

[25] Lawaczeck, O., Bütefisch, K. A., and Heinemann, H.-J., 1976. "Vortex streets in the wakes of subsonic and transonic turbine cascades". *Revue Francaise de Mecanique*, pp. 9–16.

[26] Gieß, P.-A., 1994. IB 223 - 94 a 07. Internal Report.

